3

Phase-Resolved Doppler Optical Coherence Tomography

Gangjun Liu and Zhongping Chen
Beckman Laser Institute, University of California, Irvine.
Department of Biomedical Engineering, University of California, Irvine, USA

1. Introduction

Optical coherence tomography (OCT) is an emerging medical imaging and diagnostic technology developed by MIT in the 1990s [1]. OCT uses coherence optical gating to detect the intensity of back reflected or back scattered light from the sample. It is analogous to ultrasound tomography except that light instead of sound is used. OCT can provide a depth resolution of 1-20 μm, which is one to two orders of magnitude higher than that of conventional ultrasound. OCT is a non-contact, non invasive, fast imaging modality that provides real time, three-dimensional imaging capability. OCT has been valuable in applications in the field of medicine such as ophthalmology, cardiology, otolaryngology, pulmonology, urology, dentistry, and gastroenterology [2].

In OCT, imaging contrast originates from the inhomogeneities of sample scattering properties that are dependent on sample refractive indices. In many instances, especially in the early stages of disease, changes in sample linear scattering properties are small and difficult to measure. Additional contrast mechanisms are able to extend the capability of OCT. Doppler optical coherence tomography (DOCT) or optical Doppler tomography (ODT) is one kind of functional extension of OCT which combines the Doppler principle with OCT and provides *in-vivo* functional imaging of moving samples, flows and moving constituents in biological tissues.

The first report that measured localized flow velocity with coherence gating was demonstrated in 1991 [3]. The first two-dimensional *in vivo* ODT imaging was demonstrated in 1997 [4-6]. In early ODT systems, the Doppler frequency shift was obtained by a spectrogram method which used short time fast Fourier transformation (STFFT) or wavelet transformation [4-6]. However, spectrogram methods suffer from low sensitivity and are limited for imaging speed. Phase-resolved ODT (PRODT) was developed to overcome these limitations. This method uses the phase change between sequential A-line scans for velocity image reconstruction [7-9]. PRODT decouples spatial resolution and velocity sensitivity in flow images and increases imaging speed by more than two orders of magnitude without compromising spatial resolution and velocity sensitivity [7]. The first demonstration of PRODT was based on time domain OCT systems [7-8]. Recently, the development of Fourier domain OCT systems have greatly improved the imaging speed and sensitivity [10-12]. Fourier domain ODT systems have been demonstrated by several groups [13-17].

In this chapter, we will review the principle of ODT. Due to the high velocity sensitivity of phase-resolved method and wide use of Fourier domain systems, we will focus on the phase-resolved Doppler method with Fourier domain OCT systems. Several important issues, such as phase stability of the system, sensitivity of the PRODT method, and sample movement induced artifacts for *in-vivo* applications are discussed. In the following section, we will introduce the Doppler principle and the PRODT principle. In section 3, we will discuss the velocity sensitivity of PRODT and the ways to improve the velocity sensitivity. In section 4, we will summarize the three divisions of PRODT methods: color Doppler, Doppler variance, and power Doppler. Specifically, we will discuss the cross-correlation based algorithm for color Doppler and Doppler variance calculations. In section 5, the bulk motion induced artifact in *in-vivo* applications will be discussed. In section 6, we will introduce the recent applications of PRODT from our group. The last section is the summary and acknowledgement.

2. Theory

2.1 The Doppler principle and ODT

ODT is based on the Doppler effect, which was proposed by Austrian physicist Christian Doppler in 1842. The Doppler effect manifests as change of frequency (or wavelength) for a wave reflected or scattered from moving objects. In ODT, the light reflected or scattered from a moving sample or moving subject inside the sample, changes its frequency or wavelength. The amount of the frequency change is related to the frequency of the incident light, the velocity of the moving sample, and the angle between the incident beam direction and the moving direction of subject (or sample). Figure 1 shows a scenario where the light hits on a moving target inside a sample (for example, a red blood cell in a blood vessel).The frequency change (or shift) of the light can be obtained with the following equation:

$$\Delta f = \frac{2v \cdot \cos(\theta)}{c} f_0 = \frac{2v \cdot \cos(\theta)}{\lambda_0} \tag{1}$$

where f_0 is the central frequency of the incident light, λ_0 is the central wavelength of the incident light, v is the speed of the moving target, θ is the Doppler angle (angle between the incident light and the target moving direction), c is the light speed in vacuum.

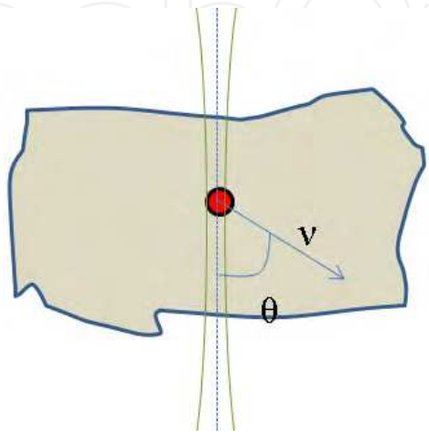

Fig. 1. Schematic of the interaction of wave and moving target inside sample .

2.2 Extraction of Doppler frequency change (shift) in ODT

In early time domain systems, the Doppler frequency shift Δf was obtained by a spectrogram method that uses the short time fast Fourier transformation (STFFT) or wavelet transformation [4-5]. In the spectrogram method, the velocity sensitivity is inversely proportional to the short-time Fourier transform window size, and the spatial resolution is proportional to the short-time Fourier transform window size [8]. Consequently, velocity sensitivity and spatial resolution are coupled. A large pixel time-window size increases velocity sensitivity while decreasing spatial resolution. In addition, the velocity sensitivity decreases with the increasing of frame rate in the spectrogram method [8]. In 2000, Zhao et al. proposed a phase-resolved method to overcome these limitations [8]. In PRODT, the Doppler frequency shift Δf is obtained by the phase change between sequential A-scans. The phase information of the fringe signal can be determined from the complex analytical signal $A_{j,z}$, where $A_{j,z}$ is the complex data at j_{th} A-scan and depth of z. The Doppler frequency shift Δf can be expressed as:

$$\begin{aligned}\Delta f &= \frac{d\phi}{2\pi \cdot dt} \\ &= \frac{\phi_{j+1,z} - \phi_{j,z}}{2\pi \cdot \Delta T} \\ &= \frac{\arg(A_{j+1,z} A_{j,z}^{*})}{2\pi \cdot \Delta T} \\ &= \frac{\tan^{-1}\left(\frac{\mathrm{Im}(A_{j+1,z})}{\mathrm{Re}(A_{j+1,z})}\right) - \tan^{-1}\left(\frac{\mathrm{Im}(A_{j,z})}{\mathrm{Re}(A_{j,z})}\right)}{2\pi \cdot \Delta T}\end{aligned} \tag{2}$$

where ΔT is the time difference between j_{th} A-scan and $(j+1)_{th}$ A-scan. In the time domain ODT system, the complex analytical signal $A_{j,z}$ is determined through analytic continuation of the measured interference fringes function by use of a Hilbert transformation. In Fourier domain ODT systems, the complex signal $A_{j,z}$ is obtained through the Fourier transformation of the acquired fringe. In this chapter, we will focus on Fourier domain PRODT systems. There are two kinds of Fourier domain ODT systems; the spectrometer-based and the swept source laser based ODT. Because the spectrometer-based ODT system shows higher phase stability and no additional phase correction is needed, we will demonstrate most of the experiments with the spectrometer-based system.

The schematic of a spectrometer-based ODT system setup demonstrated in this chapter is shown in Fig. 2. The spectrometer-based FDODT uses a super luminescent diode (SLD) light source which has a central wavelength of 890 nm and full width at half maximum (FWHM) bandwidth of 150 nm. A complementary metal–oxide–semiconductor (CMOS) based linescan camera (Sprint spL4096-70k, Basler vision technique) is used as detector. The CMOS integration time and line period are variable according to different demonstrations. The imaging process includes background signal subtraction, linear interpolation to convert data from the linear wavelength space to the linear wavenumber space, and fast Fourier transformation (FFT). The amplitude of the complex analytical signal obtained after the FFT

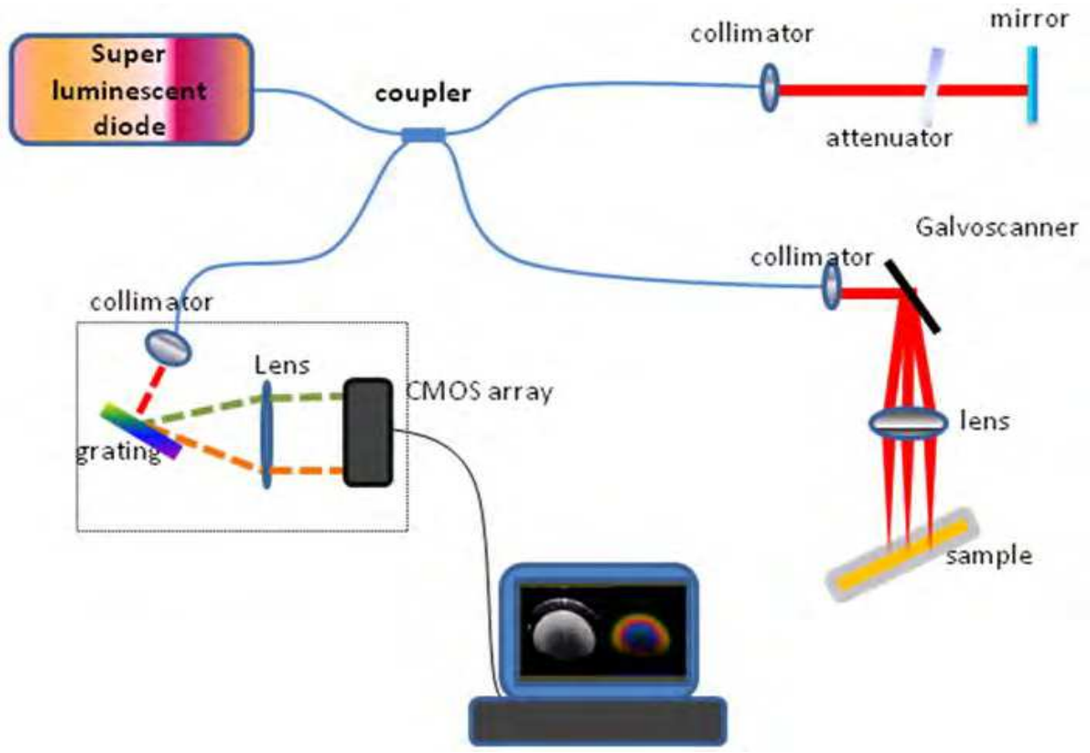

Fig. 2. Schematic of a spectrometer-based ODT system setup.

is used for OCT structure image and the PRODT images are obtained from the phase of the complex analytical signal. Figures 3(a)-(c) show the OCT images of a flow phantom. Figures 3(d), (e) and (f) show the PRODT images corresponding to Figs. 3(a), 3(b) and 3(c). The integration time was set at 47 μs and the line period was set at 50 μs. The flow phantom is made of 1% intralipid in a 500 μm diameter tube. The flow is controlled by a syringe pump. The images contain 1500 A-lines. For Fig. 3(a), 3(b) and 3(c), the angle between the tube and imaging beam was set at around 90 degrees, 85 degrees and 80 degrees, respectively, and the syringe pump speed was kept as constant. From these figures, we can verify that the Doppler frequency shift (which is proportional to the phase changes) is related to the Doppler angle. As shown in Fig. 3(a), the Doppler frequency shift is close to zero when the Doppler angle is close to 90 degrees. The Doppler frequency shift increases with the decrease of the Doppler angle (assuming the Doppler angle is between 0 degrees and 90 degrees). It should be noted that the phase is wrapped in Fig. 3(f). The velocity distribution profiles can also be determined from the PRODT images. The axial velocity distributions along white double arrow direction in Figs. 3(e) and 3(f) are shown in Fig. 4. From Eq. (1), we can also find that the Doppler frequency shift is proportional to the flow velocity if the Doppler angle is fixed. In order to verify that, we keep the angle between the incident beam and the tube constant while changing the pump speed. Figures 5 (a), (b), (c) and (d) are OCT structure images of the flow phantom pumped at, respectively, 20 μl/min, 40 μl/min, 60 μl/min, 80 μl/min. Figures 5(e), 5(f), 5(g) and 5(h) are the PRODT images of flow phantom pumped at, respectively, 20 μl/min, 40 μl/min, 60 μl/min, 80 μl/min. It should be noted that the phase is wrapped in Fig. 5(f). The increasing Doppler frequency shift with the increasing pumping speed can be clearly seen from the PRODT images.

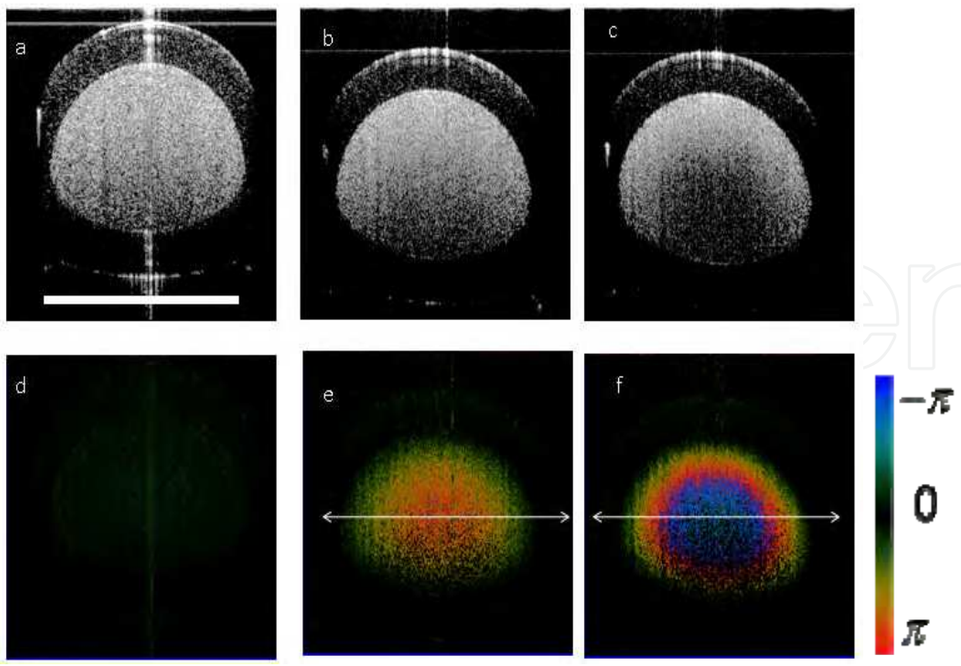

Fig. 3. (a), (b),(c) are OCT structure images of the flow phantom at a Doppler angle of around 90 degrees, 85 degrees and 80 degrees; (d), (e) and (f) are the PRODT images of the flow phantom at a Doppler angle of around 90 degrees, 85 degrees and 80 degrees. Scale bar: 500μm.

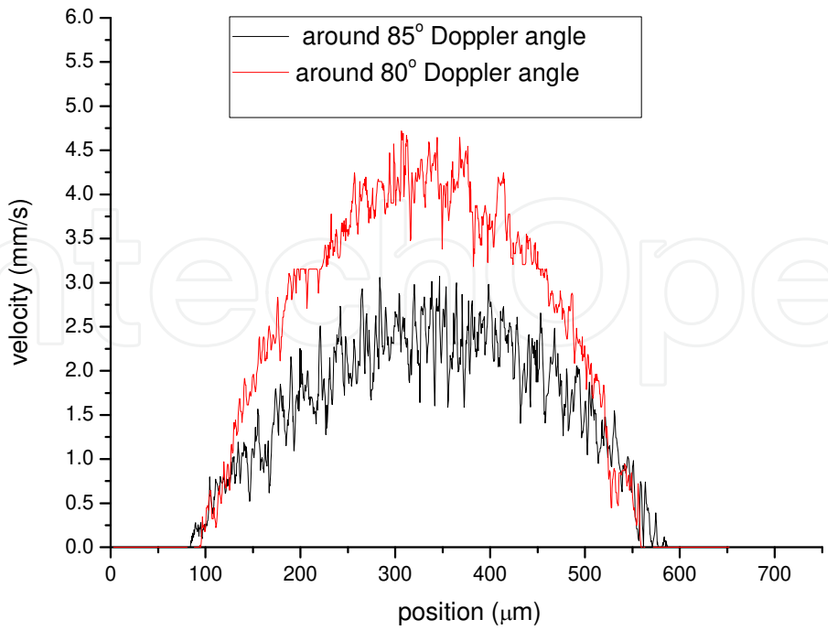

Fig. 4. Velocity profile along the double arrows in Figs. 3(e) and 3(f).

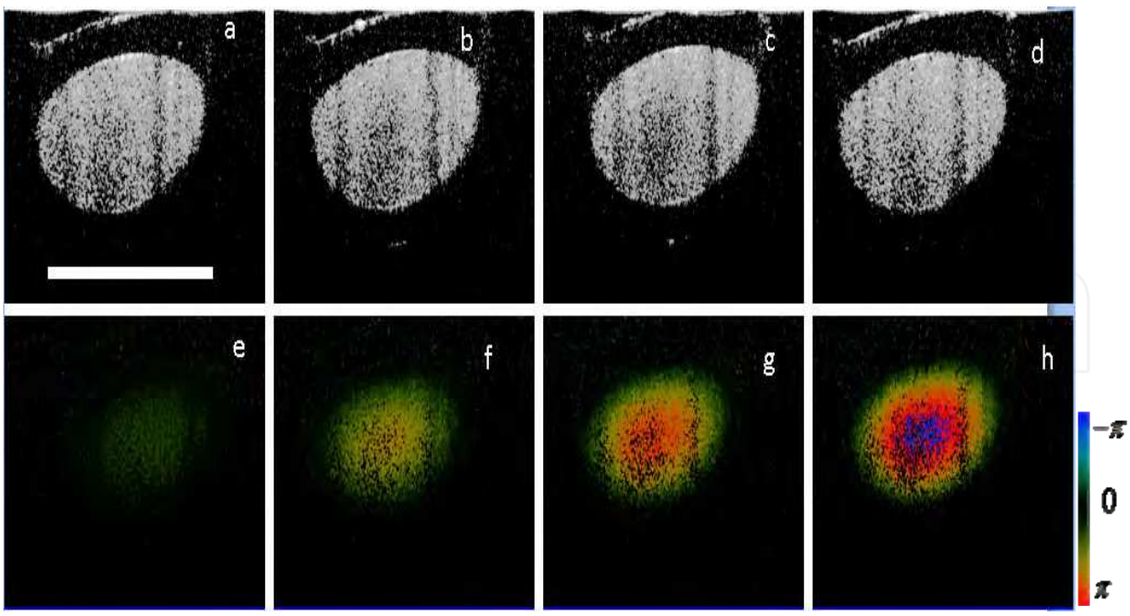

Fig. 5. (a), (b), (c) and (d) are OCT structure images of the flow phantom pumped at, respectively, 20μl/min, 40μl /min, 60μl /min, 80μl /min; (e), (f), (g) and (h) are the PRODT images of the flow phantom pumped at, respectively, 20μl /min, 40μl /min, 60μl /min, 80μl /min. Scale bar: 500μm.

3. Sensitivity of PRODT and minimum detectable Doppler shift

From Eqs. (1) and (2), the velocity of the sample can also be obtained. The minimum resolvable velocity of the system is decided by the minimum resolvable phase difference and the velocity may be expressed as:

$$v_z = \frac{\lambda_c \cdot \delta\theta}{4\pi \cdot n \cdot \Delta T} \tag{3}$$

where v_z is the velocity along the incident beam direction, λ_c is the central wavelength of the OCT system, n is the refraction index of the sample, ΔT is the time difference between adjacent A-lines, and $\delta\theta$ is the minimum resolvable phase difference. Typical phase stability for a spectrometer-based FDOCT is a few milliradians. For swept source based FDOCT, the phase stability can also reach a few milliradians to tens of milliradians range after phase correction. Assuming the A-line rate of the OCT system is 100,000 A-lines per second, the phase stability of the system is 10 milliradians and the refraction index is 1.4, the minimum velocity (along the incident beam direction) that can be resolved by an ODT system with a central wavelength of 1.3 μm is around 74 μm/s.

PRODT has been widely used for *in-vivo* imaging of blood flow in animal or human being. For these applications, the Doppler angle and blood flow velocity are usually unknown in advance. If we assume the velocity of the sample and the Doppler angle are unknown, the minimum detectable Doppler frequency shift is decided by the minimum resolvable phase difference ($d\phi$) and the time difference ΔT in Eq. (2). The minimum resolvable phase difference for an ODT system is related to the phase stability of the system that is affected by

factors such as mechanical stability of the system and image SNR. The phase stability of the system can be determined by statistically analyzing the adjacent A-line phase difference of a static mirror. Figure 6(a) shows the measured phase difference of a static mirror by the spectrometer-based Fourier domain ODT system described in the previous section. The integration time was set as 22 μs and the line period was set as 25 μs, which corresponds to an A-line speed of 40,000 Hz. Figure 6(b) shows the histogram of the phase difference distribution. The phase stability is the standard deviation for the histogram of the phase difference distribution. The histogram shows a Gaussian shape-like profile with a FWHM value of 20 milliradians. In order to improve the velocity sensitivity of the PRODT system, increasing the phase stability of the system is necessary. Because there are no mechanical moving parts in the spectrometer-based Fourier domain systems, spectrometer-based Fourier domain systems usually show high phase stability. Most of the demonstrated PRODT systems use spectrometer-based Fourier domain systems.

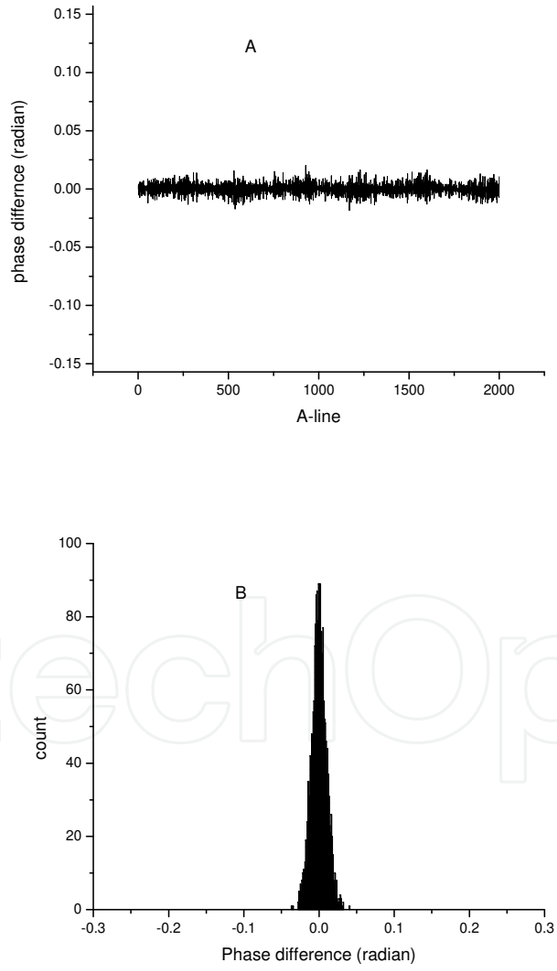

Fig. 6. Phase stability analysis of the spectrometer-based OCT system. (a) Phase differences between adjacent A-lines at the static mirror location; (b). Histogram of the phase difference distribution.

Swept source OCT (SSOCT) systems usually use tunable filters that are based on mechanically scanning of galvanometer mirrors, polygon mirrors or Fabry–Pérot (FP) filters. Due to the mechanical scanning schemes used, swept source OCT systems usually show worse phase stability than spectrometer-based OCT systems. If phase sensitive methods are used, the phase must be corrected before using the phase-resolved algorithm [16-19]. Here, we tested the phase stability of a SSOCT system. The system used a MEMS technique-based swept source laser with a central wavelength of 1310 *nm*, an FWHM spectral bandwidth of about 110 *nm* , an A-line rate of 50,000 Hz, and a total average power of 16 mW (SSOCT-1310, Axsun Technologies Inc, Billerica, MA). The system used a Mach-Zehnder type interferometer with 90% of the light in the sample arm and 10% of the light in the reference arm. A dual-balanced detection scheme was used to acquire the signal. The system works in the K-trigger mode so that no re-calibration is needed. In order to analyze the phase stability of the SSOCT system, a static mirror was used as a sample, and phase differences between adjacent A-lines at the mirror location were obtained. Figure 7(a) shows the phase difference distribution and Fig. 7(b) shows the histogram of the phase difference distribution. Although the histogram as in Fig. 7(b) shows a Gaussian-like profile with an FWHM value of 0.18 radians, there are lots of counts at the large phase difference location. This can be seen more clearly in Fig. 7(a) that shows a lot of phase jumping between adjacent A-lines. These results indicate that spectrometer-based OCT systems show much better phase stability as demonstrated in Fig. 6.

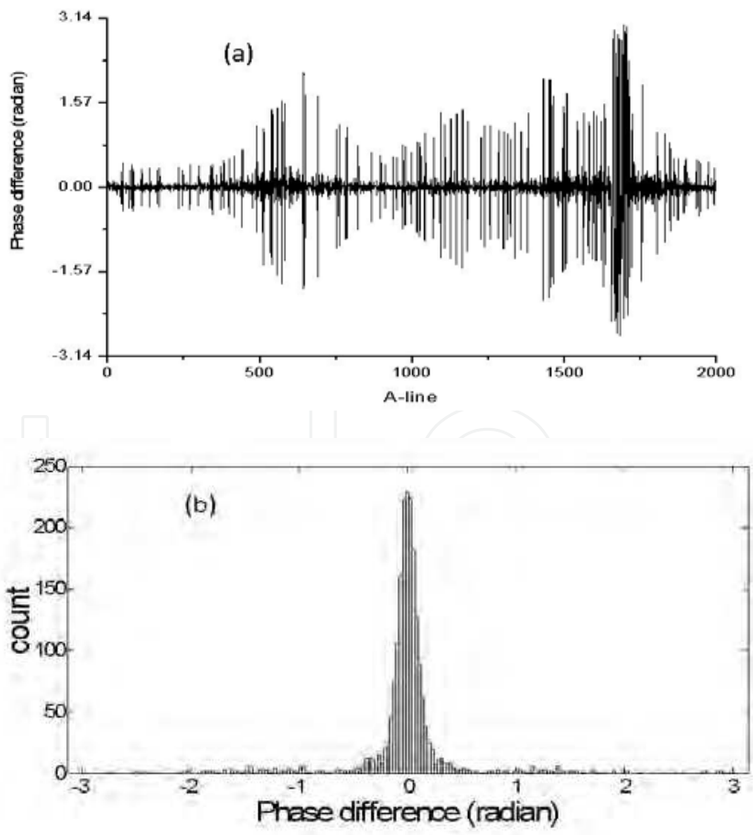

Fig. 7. Phase stability analysis of the SSOCT system. (a) Phase differences between adjacent A-lines at the static mirror location; (b) histogram of the phase difference distribution [20].

There are a number of ways to improve Doppler detection sensitivity. A static surface may be added as a reference to correct phase error and improve the phase stability. Our group has used the top surface of chick chorioallantoic membrane (CAM) as a reference to obtain the blood flow in a CAM [16]. Vakoc et al. have proposed a method to tap 1% of the sample arm light and direct it at a calibration mirror which is positioned near the maximum imaging range of the system [17]. A common-path method has been used to correct phase errors [18, 19]. Figure 8 show the effectiveness of the phase correction method [19]. The laser source is a high speed swept laser with a central wavelength of 1050 nm and a sweeping speed of 100 kHz (Axsun Technology, Billerica, MA). The laser source output is split into the reference and sample arms by a 20:80 coupler with 80% in the reference arm and 20% in the sample arm. In the reference arm, the light is further split by a 95:5 coupler. Ninety-five percent of the light in the reference is sent to cause interference with the collected back-reflection or backscattering signal from the sample. This interference signal is detected by a balanced photon detector and digitized by a high speed digitizer (ATS 9350, Alazar Technologies Inc., Pointe-Claire, QC , Canada). The remaining 5% of the light in the reference arm is sent to a non-balanced photon-detector after passing through a 1 mm thick cover slide and is then finally digitized by another channel in the digitizer [19]. The two surfaces of the cover glass will generate an inference fringe. This will produce a reference surface at a depth corresponding to the thickness of the cover glass. By subtracting a portion of the phase difference of the reference surface location from the phase difference of the sample signal, the phase error is corrected [17-19]. Figures 8(a) and 8(b) show the OCT structure image and the phase difference between successive A-lines before correction for a mirror respectively. Figure 8(c) shows the phase difference between successive A-lines after the correction. The improvement can be seen by comparing the images in Fig. 8(b) and Fig. 8(c).

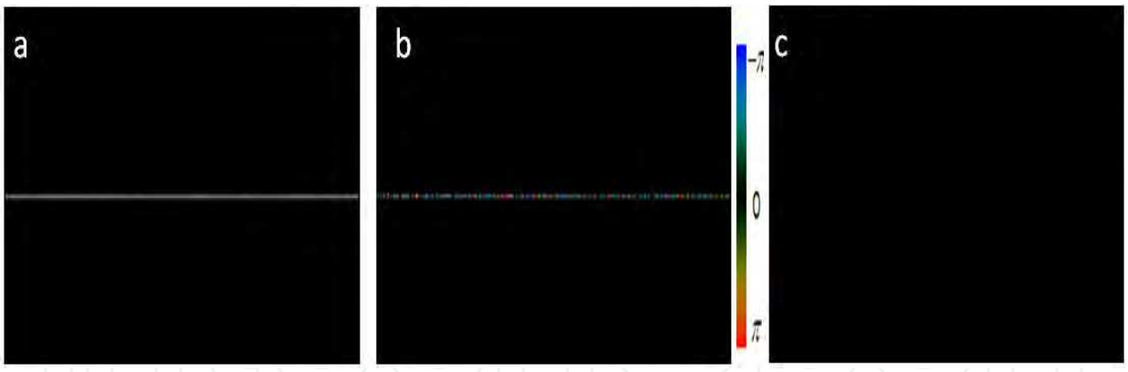

Fig. 8. (a) OCT images of a mirror; (b) adjacent A-line phase difference before correction; (c) adjacent A-line phase difference after correction [19].

Increasing the velocity sensitivity by improving the phase stability is effective. The typical phase stability of spectrometer-based ODT or SSOCT after phase correction will be a few milliradians. The biological tissue will produce adjacent A-line phase changes due to optical heterogeneity of the tissue [21, 22]. This heterogeneous index change will cause phase noise in the PRODT images. In addition, any mechanical movement from the system or environment may introduce phase noise in the PRODT images. These introduced phase noise may be larger than the phase stability of the system. Therefore, the velocity sensitivity may be determined by the phase noise instead of the system phase stability.

Another effective way to increase the velocity sensitivity is to increase the ΔT , namely decrease the A-line speed. From Eq. (3), we can find that the minimum resolvable velocity is inversely proportional to ΔT when all other parameters remain unchanged. Figure 9 shows OCT and PRODT images of a flow phantom acquired by a system with a different A-line rate. The system was the CMOS spectrometer-based FDOCT system described in previous section (Fig. 2). The flow phantom was pumped by the syringe pump at a constant speed for all of the setups. The Doppler angle was the same for all of the setups and it was fixed to be different from 90 degrees so that the Doppler frequency shift was not zero. Figures 9(a)-9(d) show the OCT images of the flow phantom. In Figures 9(a), 9(b), 9(c) and 9(d), the integration time of the CMOS camera was kept as constant (22 μs in this case) while the line periods were set as 25 μs, 50 μs, 100 μs and 200 μs, respectively. The effective A-line rates for Fig. 9(a), 9(b), 9(c) and 9(d) were, respectively, 40,000 Hz, 20,000 Hz, 10,000 Hz and 5,000 Hz. Figures 9(e), 9(f), 9(g) and 9(h) are the PRODT images of the flow phantom corresponding to the OCT images in Figs. 9 (a), 9(b), 9(c) and 9(d). The effectiveness of increasing the velocity sensitivity by reducing the A-line rates can be seen from the PRODT images in Fig. 9.

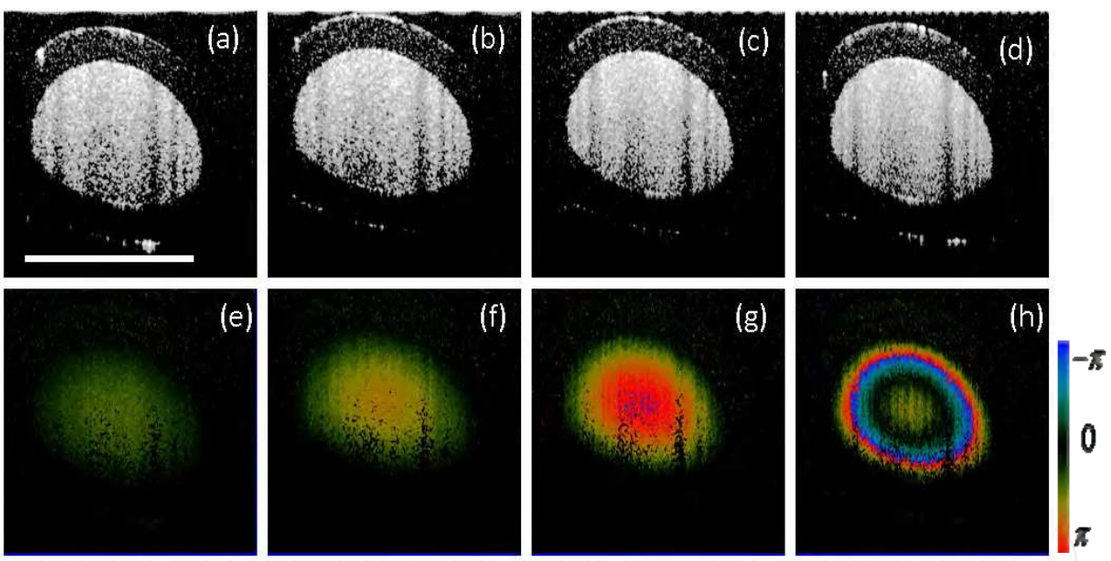

Fig. 9. (a), (b), (c) and (d) are OCT structure images of the flow phantom imaged with the line period set as, respectively, 25 μs, 50 μs, 100 μs and 200 μs; (e), (f), (g) and (h) are the PRODT images of flow phantom obtained with the detector line period set as, respectively, 25 μs, 50 μs, 100 μs and 200 μs. Scale bar: 500μm.

Although changing the A-line rate is an effective way to improve the velocity sensitivity of the PRODT system, faster A-line speed is always preferred so that the imaging time is reduced. Faster speed is especially important for real time or *in-vivo* imaging applications. Increasing the velocity sensitivity without sacrificing the A-line rate can be achieved by extending the phase-resolved algorithms to non-adjacent A-lines while still maintaining space correlation. In this way, the velocity sensitivity of the PRODT is improved while the A-lines speed is still maintained. For such cases, we can rewrite Eq. (2) as follows:

$$\Delta f = \frac{d\phi}{2\pi \cdot dt} = \frac{\phi_{m,z} - \phi_{n,z}}{2\pi \cdot \Delta T(m,n)} = \frac{\tan^{-1}\left(\frac{\mathrm{Im}(A_{m,z})}{\mathrm{Re}(A_{m,z})}\right) - \tan^{-1}\left(\frac{\mathrm{Im}(A_{n,z})}{\mathrm{Re}(A_{n,z})}\right)}{2\pi \cdot \Delta T(m,n)} \tag{4}$$

where $A_{m,z}$ is the complex data at m_{th} A-scan and depth of z , $A_{n,z}$ is the complex data at n_{th} A-scan and depth of z, and $\Delta T(m,n)$ is the time difference between m_{th} A-scan and n_{th} A-scan. When using the above algorithm, the spatial correlation between m_{th} A-scan and n_{th} A-scan should be maintained. Figure 10 shows a way to realize this scheme. Black dots in Fig. 10 show beam scanning locations in a traditional raster scanning pattern. The horizontal direction is the fast galvomirror scanning direction and the vertical direction is the slow galvomirror scanning direction. The three points (m , $m+1$ and n , indicated by the red arrows) indicate 3 locations of the OCT A-scan. Traditional phase-resolved algorithms calculate the Doppler shift with the phase difference between adjacent scanning point m and point $m+1$ at a time difference of $\Delta T(m,m+1)$. However, if the algorithm is used between points m and n , the ΔT is increased greatly because $\Delta T(m,n)$ is much larger than$\Delta T(m,m+1)$. Consequently, the minimum detectable velocity is also increased according to Eq. (3). This scheme has been adopted by several groups to image microsvascular networks [23-25]. Another method extending ΔT is to use a dual beam setup [26, 27]. Two tomograms which are slightly separated in time are obtained from the two beams that are spatially offset. The PRODT algorithm is performed between these two data sets. In this way, the $\Delta T(m,n)$ is tunable by tuning the space offset of the two beams.

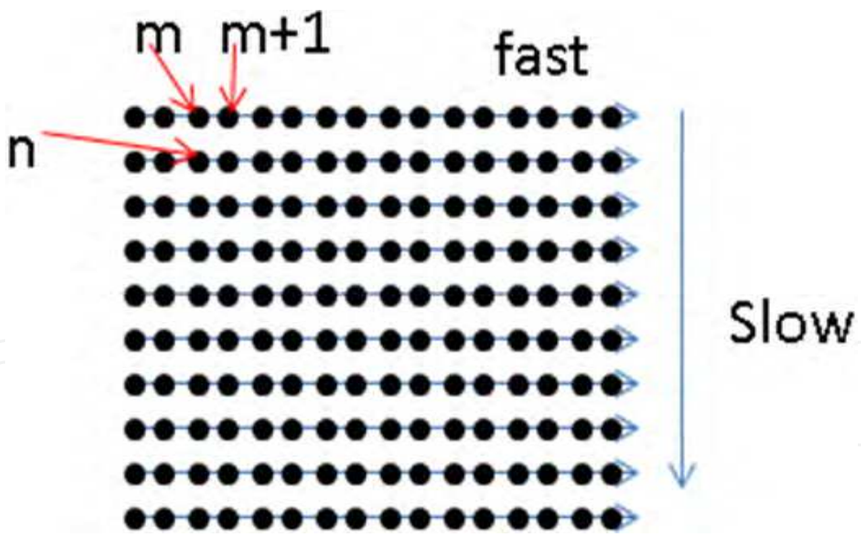

Fig. 10. Schematic of inter-frame processing scheme for PRODT.

4. Cross-correlation algorithm for PRODT, Doppler variance and power Doppler methods

ODT techniques have been widely used for flow imaging, especially blood flow in animals or human beings. Blood flow in humans or animals is complex, and the flow is pulsatile. The flow speed in a blood vessel is not a constant value and changes from the center of the blood

vessel to the edge. A parabolic equation may describe the distribution of the steady blood flow along the blood vessel radius. This kind of steady flow is usually called laminar flow. Laminar flow may breakdown into a turbulent flow when the velocity becomes sufficiently high [28]. In practice, the Doppler frequency produced by a single target will produce a spectrum of Doppler frequencies or a series of frequency shifts instead of a single frequency. This spectrum broadening is attributed to several sources, such as the cone-geometrical focusing beam, Brownian motion and speckle. Brownian motion dominates the broadening of the Doppler spectrum at low flow speed, and probe-beam geometry dominates at high flow speed [29].

Depending on the Doppler frequency shift information obtained, we can display this information in a color Doppler method or a variance method. In the color Doppler imaging method, the average Doppler frequency shift is displayed as color images, and the negative and positive averaged frequency shifts are displayed in different colors [4-6,8,9], which provide quantitative information on the flow speed and flow direction. In a Doppler variance image, the variance or the standard deviation of the Doppler frequency shift is displayed [7], which can be used to quantify Brownian motion or measure transverse flow [29].

In addition, there is a power Doppler mode that displays the flow power signal by filtering out the signal form stationary tissue [30]. In Fourier domain OCT systems, the filtering process may be realized by hardware-based or software-based methods. Wang et al. developed a method called optical microangiograph (OMAG) [31-35]. In OMAG, a Doppler frequency is introduced in the lateral beam scanning direction (B-scan) so that the moving and static scattering components within the sample are separated. The Doppler frequency may be introduced by either the reference mirror mounted on A-linear piezo translation stage or by offsetting the sample arm beam from the scanning galvomirror pivot. Yuan et al. proposed a digital frequency ramping method by numerically introducing a phase shift into the original spectral interferometric signal using a Hilbert transform [36]. Tao et al. proposed single-pass flow imaging spectral domain optical coherence tomography (SPFI-OCT) with a modified Hilbert transform algorithm to separate moving and non-moving scatters [37, 38].

Instead of using the algorithm as in Eqs. (2) and (4) directly, the algorithm derived from a cross-correlation algorithm shows better performance and is usually preferred [7-9, 39, 40]. In addition, averaging can improve the signal noise ratio [7-9, 40]. Averaging could be performed in the lateral direction (temporal direction) so that the Eqs. (2) and (4) can be rewritten as [8]:

$$\overline{f} = \frac{1}{(2\pi \cdot \Delta T)} \arctan\left\{ \frac{\sum_{j=1}^{J}\left[\mathrm{Im}(A_{j+1,z})\mathrm{Re}(A_{j,z}) - \mathrm{Im}(A_{j,z})\mathrm{Re}(A_{j+1,z}) \right]}{\sum_{j=1}^{J}\left[\mathrm{Re}(A_{j,z})\mathrm{Re}(A_{j+1,z}) + \mathrm{Im}(A_{j+1,z})\mathrm{Im}(A_{j,z}) \right]} \right\} \tag{5}$$

where J is the number of A-lines that are averaged. Averaging could also be performed in both lateral and depth directions and Eqs. (2) and (4) become [18, 19, 20]:

$$\bar{f} = \frac{1}{(2\pi \cdot \Delta T)} \cdot \arctan\left\{ \frac{\sum_{j=1}^{J}\sum_{z=1}^{N}\left[\mathrm{Im}(A_{j+1,z})\mathrm{Re}(A_{j,z}) - \mathrm{Im}(A_{j,z})\mathrm{Re}(A_{j+1,z})\right]}{\sum_{j=1}^{J}\sum_{z=1}^{N}\left[\mathrm{Re}(A_{j,z})\mathrm{Re}(A_{j+1,z}) + \mathrm{Im}(A_{j+1,z})\mathrm{Im}(A_{j,z})\right]} \right\} \tag{6}$$

where J is the number of A-lines that are averaged, and N is the number of depth points that are averaged. The choice of J and N are dependent on application. Generally, a larger J and N will increase SNR, increase the computing time, and decrease resolution.

Doppler variance uses the variance of the Doppler frequency spectrum to map the flow. Doppler variance has the benefit of being less sensitive to the pulsatile nature of the blood flow, less sensitive to the incident angle, and may be used to obtain the transverse flow velocity [7, 29, 41, and 42]. If σ denotes the standard deviation of the Doppler spectrum, the Doppler variance σ^2 can be obtained [7]:

$$\sigma^2 = \frac{\int (f - \bar{f})^2 P(f) df}{\int P(f) df} = \overline{f^2} - \bar{f}^2 \tag{7}$$

where $\bar{f}$ is Doppler frequency and $P(f)$ is the power spectrum of the Doppler frequency shift. With the help of autocorrelation technology, the variance can be expressed as [7]:

$$\sigma^2 = \frac{1}{(2\pi \cdot \Delta T)^2}\left(1 - \frac{\left|A_{j+1,z}A_{j,z}^*\right|}{A_{j,z}A_{j,z}^*}\right) \tag{8}$$

where $A_{j,z}^*$ is the complex conjugate of $A_{j,z}$ .Similar to the color Doppler algorithms in Eqs. (5) and (6) , averaging is usually used to improve the SNR and we have:

$$\sigma^2 = \frac{1}{(2\pi \cdot \Delta T)^2}\left[1 - \frac{\left|\sum_{j=1}^{J}\left(A_{j+1,z}A_{j,z}^*\right)\right|}{\sum_{j=1}^{J}\left(A_{j,z}A_{j,z}^*\right)}\right] \tag{9}$$

$$\sigma^2 = \frac{1}{(2\pi \cdot \Delta T)^2}\left[1 - \frac{\left|\sum_{j=1}^{J}\sum_{z=1}^{N}\left(A_{j+1,z}A_{j,z}^*\right)\right|}{\sum_{j=1}^{J}\sum_{z=1}^{N}\left(A_{j,z}A_{j,z}^*\right)}\right] \tag{10}$$

where J is the number of A-lines that are averaged and N is the number of depth points that are averaged.

Figure 11 shows images of the hamster skin installed in a dorsal window chamber. The images are obtained with a charge-coupled device (CCD) spectrometer-based OCT system

[42]. Figures 11(a), 11(b), 11(c) and 11(d) show the OCT structure image, color Doppler image, Doppler variance image and power Doppler image, respectively. The color Doppler image and Doppler variance image are obtained with the Eqs. (6) and (10), respectively, with $J = 4$ and $N = 4$. The power Doppler image is obtained with a modified Hilbert method [24, 37]. From the figures, it can be found that all three methods are able to detect the blood vessels. However, the information they provide are different and this information are actually complementary. Color Doppler can give information regarding the flow direction and the speed of the flow. Doppler variance provides flow turbulence information and transverse flow velocity. Power Doppler provides the total power of the Doppler signal from the flows.

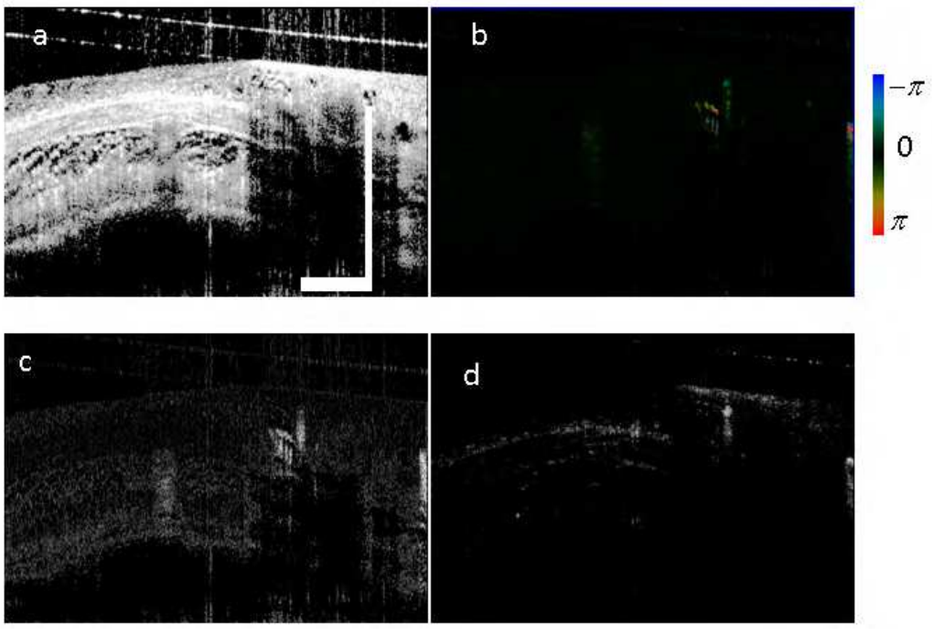

Fig. 11. OCT images of the hamster skin installed in a dorsal window chamber. (a) OCT structure image; (b) color Doppler image; (c) Doppler variance image; (d) power Doppler image. Scale bar: 500 μm.

5. Bulk-motion and *in-vivo* imaging

Because of its high spatial resolution and velocity sensitivity, Doppler OCT has been widely used for blood flow related biomedical applications [32-25, 41-48]. These applications require imaging of blood flow *in-vivo*. For *in-vivo* applications, especially awake patient imaging, axial sample movement induced by involuntary movements will introduce bulk-motion and change the Doppler frequency [9]. Both sample movement and blood flow inside the tissue will change the reflected or scattered light frequency. The Doppler frequency in the blood vessels obtained with phase-resolved method will be a linear sum of the Doppler frequency induced by the sample movement and actual blood flow [9]. Figures 12(a) and 12(b) show the *in-vivo* OCT structure and PRODT images of human retina obtained with a CCD spectrometer-base FDOCT system [41, 42, and 45]. The ODT image shows strong bulk-motion induced artifact which manifests as strong background noise, especially around the leftmost and rightmost regions in the yellow circles of Fig. 12(b). The

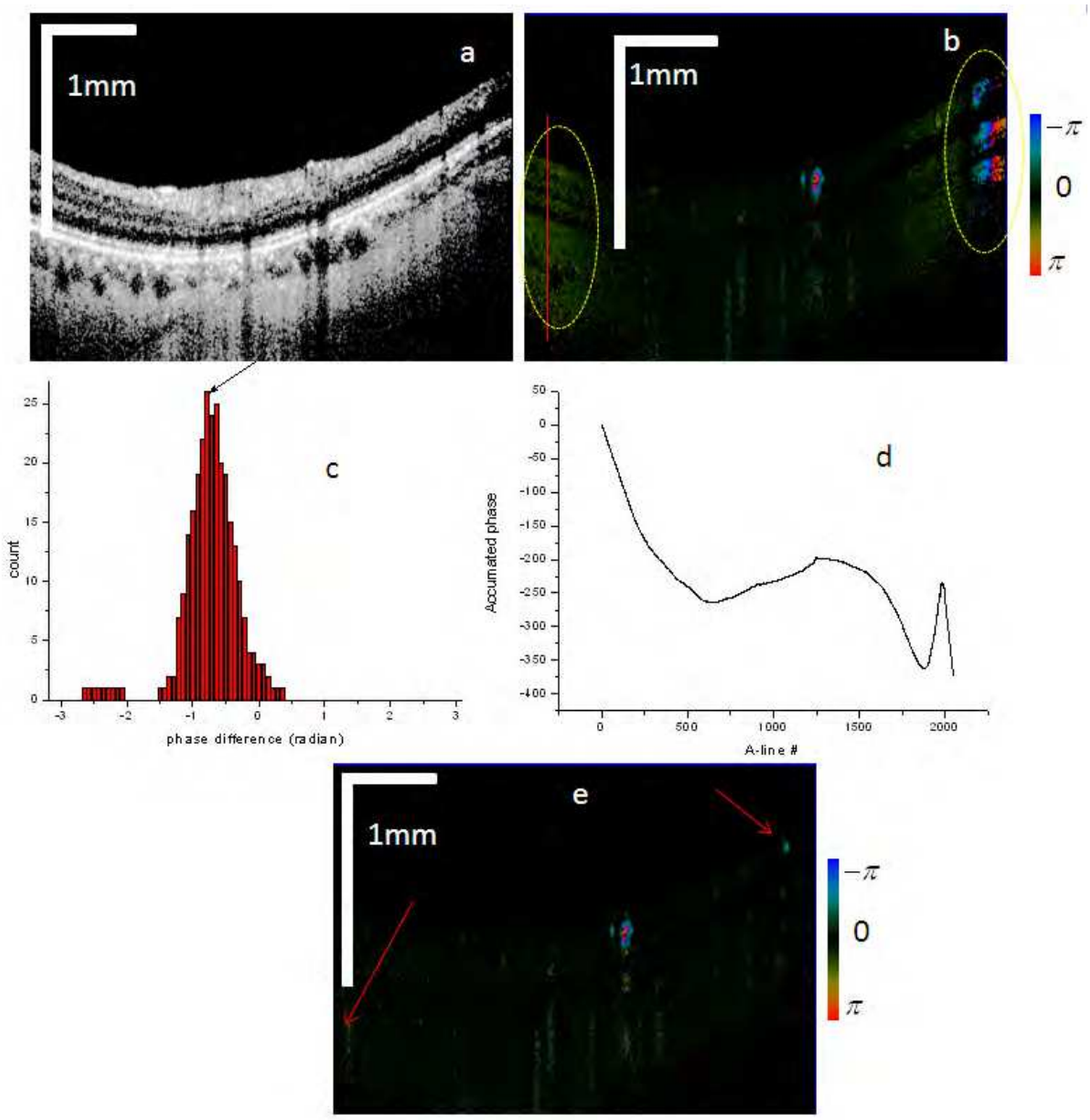

Fig. 12. Demonstration of bulk-motion correction for *in-vivo* PRODT application. (a) *In-vivo* OCT structure and (b) PRODT images without bulk-motion correction of human retina; (c) histogram of the phase difference distribution for the A-line indicated by the red vertical line in Fig.12(b); (d) accumulated bulk-motion phase of all the A-lines; (e) PRODT images with bulk-motion correction.

blood vessels in these regions are not able to be identified from the PRODT image. In order to obtain the Doppler frequency induced by the actual blood flow, the Doppler frequency induced by the sample movement must be identified and subtracted. The sample movement may be considered as a "global" effect; it will induce constant Doppler shift for the whole A-line. Most bulk-motion correction methods assume that the sample movement will induce a constant phase term for each A-line, and by subtracting this phase term, the bulk-motion induced artifacts can be corrected [9, 32, 40 and 49]. Up to now, several methods have been proposed to determine the bulk phase [9, 32, 40, 41 and

49]. Usually, the median phase or mean phase is determined from a histogram of adjacent A-line phase differences and then subtracted. Recently, averaged shift histogram-based nonparametric density estimators have shown good performance and have become popular in extracting the bulk phase [32, 41 and 49]. Figure 12(c) shows the histogram of the phase difference distribution for the A-line indicated by the red vertical line in Fig. 12(b). The location with the maximum bin count as indicated by the black arrow is taken as the bulk phase. By repeating this process for all the A-lines in the B-scan image, the bulk phases for all the A-lines are draw as Fig. 12(d). The phases in Fig. 12(d) are unwrapped and then subtracted from the phases of the corresponding A-line. Figure 12(e) shows the PRODT images after the phase-correction method has been used. The blood vessels that cannot be identified in Fig. 12 (b) are clearly visible in Fig. 12(e). The red arrows in Fig. 12(e) indicate two such vessels.

These histogram-based methods have shown success in different situations and been applied for color Doppler and OMAG [23, 32, 41 and 49]. However these methods increase the computational complexity and time. The correction may also introduce artifacts when the blood vessels are large and take most of the pixels for an A-line [35, 45]. We have shown that the Doppler variance method is not sensitive to bulk-motion and the method can be used without correcting the bulk-motion when the sample-movement-induced velocity changes gradually [42].

If ϕ_j is the bulk phase induced by sample movement at the jth A-line, when there is sample movement, we can rewrite Eq. (2) as

$$\begin{aligned} \bar{f} &= \arg(A_{j+1,z}\exp(i\phi_{j+1}\,A^*_{j,z}\exp(-i\phi_j))/(2\pi\cdot\Delta T) \\ &= \arg(A_{j+1,z}A^*_{j,z})/(2\pi\cdot\Delta T)+\Delta\phi_j/(2\pi\cdot\Delta T) \end{aligned} \tag{11}$$

where $\Delta\phi_j=\phi_{j+1}-\phi_j$ and $\Delta\phi_j/T$ is the Doppler frequency shift induced by the axial direction sample movement. Therefore, when there is axial sample movement, the average Doppler frequency shift detected is the linear sum of the Doppler frequency shift induced by sample movement with the Doppler frequency shift without sample movement.

However, for the Doppler variance, we can rewrite Eq. (8) as follows when there is sample movement,

$$\begin{aligned} \sigma^2 &= \frac{1}{(2\pi\cdot\Delta T)^2}\left(1-\frac{\left|A_{j+1,z}\exp(i\phi_{j+1}\,A^*_{j,z}\exp(-i\phi_j\right|}{A_{j,z}A^*_{j,z}}\right) \\ &= \frac{1}{T^2}\left(1-\frac{\left|A_{j+1,z}A^*_{j,z}\right|}{A_{j,z}A^*_{j,z}}\right). \end{aligned} \tag{12}$$

We can find that the Doppler variance is only a function of the amplitude of the signal and not related to the phase term of the signal. In the case where lateral averaging is used as in Eq. (9), we can rewrite it as follows when there is sample movement:

$$\sigma^2 = \frac{1}{(2\pi \cdot \Delta T)^2}\left[1 - \frac{\left|\sum_{j=1}^{J}\left(A_{j+1,z}A_{j,z}^{*}\right)\exp(i\Delta\phi_j)\right|}{\sum_{j=1}^{J}\left(\left|A_{j,z}\right|^2\right)}\right] \tag{13}$$

where $\Delta\phi_j = \phi_{j+1} - \phi_j$ and $\Delta\phi_j$ is proportional to the velocity of the axial direction sample movement. Eq. (13) can also be written as

$$\sigma^2 = \frac{1}{(2\pi \cdot \Delta T)^2}\left[1 - \frac{\left|\sum_{j=1}^{J}\left(A_{j+1,z}A_{j,z}^{*}\right)\exp(i\Delta\phi_j - i\Delta\phi_1)\right|}{\sum_{j=1}^{J}\left(\left|A_{j,z}\right|^2\right)}\right] \tag{14}$$

where $\Delta\phi_j = \phi_{j+1} - \phi_j$ and $\Delta\phi_j$ is proportional to the velocity of the axial direction sample movement. Therefore, when there is sample movement and Eq. (9) is used to calculate the Doppler variance, the value of the variance is a function of $\Delta\phi_j - \Delta\phi_1$, which is proportional to the sample-movement-induced velocity difference between the 1st A-line and the other A-lines in the averaging area. For most *in-vivo* applications, the velocity induced by sample movement changes gradually and this velocity difference in the small averaging area (usually 4-16 A-lines) is small. When both lateral and depth averaging algorithms are used as in Eq. (10), the impact of sample movement on the Doppler variance is reduced further (by N times) because ϕ_j is assumed to be constant in a single A-line.

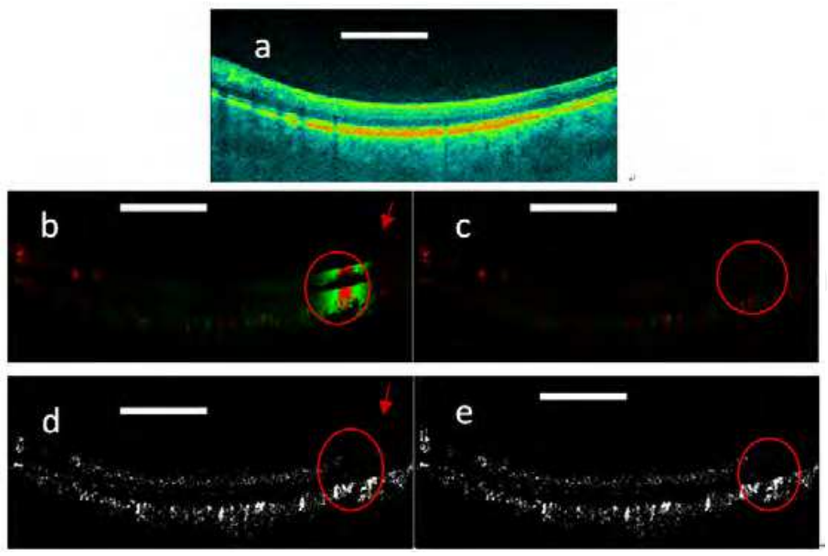

Fig. 13. (a) OCT intensity image; (b) color Doppler OCT image without bulk-motion correction; (c) color Doppler OCT image with bulk-motion correction; (d) Doppler variance OCT image without bulk-motion correction; (e) Doppler variance OCT image with bulk-motion correction. Scale bar: 1mm [42].

Figure 13 shows the OCT images of the human retinal region. The images shown have a scanning range of $5\,mm$ and include 2048 A-lines. Figure 13(a) shows the OCT structural image. Figures 13(b) and 13(c) show color Doppler images with and without bulk phase correction. Figures 13(d) and 13(e) show the Doppler variance images with and without bulk phase removal.

From Fig. 13(b), it can be seen that the color Doppler image is affected by bulk-motion. The bulk-motion increases the background signal of the color Doppler image and blood vessels cannot be identified if the bulk-motion is too strong, as shown in the region inside the red circle in Fig. 13(b). It can also be found that the bulk phase induced by bulk-motion is constant along the axial direction, which is the basis of the current bulk-motion algorithm. This also proves that the Doppler frequency induced bulk-motion can be considered as a constant variable in a single A-line. Sample movement induced motion artifacts must be corrected before applying the color Doppler algorithm. The bulk-motion-corrected image as demonstrated in Fig. 13(c) shows great improvement, and the color Doppler image demonstrates much clearer blood vessels. However, in the region where large blood vessels exist, the bulk-motion-corrected image in Fig. 13(c) shows correction artifacts as indicated by the red arrows. Although this correction artifact is not important in most imaging areas, the artifacts may cause erroneous blood vessel locations in the color Doppler image in regions with large blood vessels such as the optic disk. An improved phase-resolved algorithm has been proposed to correct this artifact [45]. Although effective, the improved algorithm increases the calculation time.

In the Doppler variance image without bulk-motion correction as shown in Fig. 13(d), the blood vessels can be seen even in the high speed sample movement region shown in the red circle. As shown in the previous section, the Doppler variance obtained with the averaged autocorrelation algorithm is affected by the sample-movement-induced velocity difference within the averaging area. We can find from Fig. 13(b) that velocity of sample movement changes gradually (please note the green to red color change in the high speed sample movement region is due to phase wrapping). The sample-movement-induced velocity change is small in the small averaging area. Because depth averaging is also used, the bulk-motion effect can be neglected here. The Doppler variance image with bulk-motion correction is also shown in Fig. 13(e) in order to verify the results. The two images [Figs. 13(d) and 13(e)] show great similarity and the high bulk-motion region as in the circle regions. However, similar to color Doppler images, histogram-based bulk-motion-correction also introduces artifacts in the final Doppler variance image as indicated by the red arrow in Fig. 13(e). The Doppler variance image [Fig. 13(d)] without bulk-motion-correction is artifact free.

6. Recent application with PRODT

Blood flow related biomedical applications with PRODT have been demonstrated for imaging ocular blood flow, mapping cortical hemodynamics for brain research, drug screening, monitoring changes in image tissue morphology and hemodynamics following pharmacological intervention and photodynamic therapy, evaluating the efficacy of laser treatment in port wine stain (PWS) patients, assessing the depth of burn wounds, imaging tumor microenvironment, and quantifying cerebral blood flow [32-25, 41-48]. There have been excellent review papers or book chapters about the advances of PRODT [2 and 50]. We will introduce the recent applications and PRODT for application beyond the flow imaging.

Recent advances of PRODT techniques have made capillary vasculature imaging possible. Our group has demonstrated fine retina microvascular networking with color Doppler, Doppler variance and OMAG techniques [41]. Figure 14(a) shows a top view of the 3-D variance reconstruction, and Fig. 14(b) shows a color-coded variance image where the retina vessels are coded with orange and the choroid ones with blue-green. Figure 14(c) gives a 3-D Doppler reconstruction of the vasculature from which one can notice the Doppler flow "artifact" in some vessels due to the Doppler angle change labeled 1 and the pulsatile nature of the blood flow labeled 2. Figures 14(d) and 14(e) show the results of 3-D OMAG. Ultrahigh sensitive PRODT techniques with inter-frame PRODT algorithm or dual beam methods have been demonstrated for several kinds of applications [23-27].

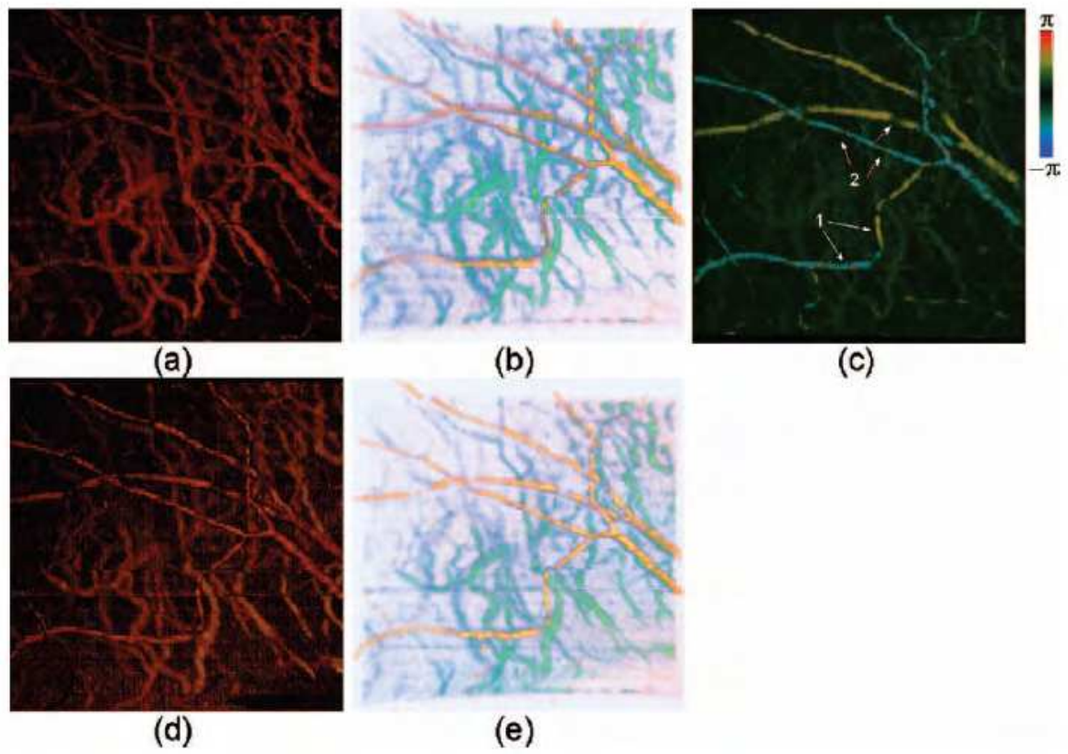

Fig. 14 Three-dimensional angiography of the human eye by different imaging modalities: (a) top view projection of 3-D variance imaging; (b) color-coded variance image; (c) 3-D ODT image; (d) and (e) show the top view and color-coded results from 3-D OMAG [41].

In addition to blood flow related applications, our group has extended the application of ODT for functional imaging of moving tissue to provide the axial direction velocity distribution in the cross-section image. Figure 15 shows the velocity distribution of a cross-sectional image obtained with the phase-resolved color Doppler method for M-Mode *ex-vivo* imaging of a vibrating swine vocal fold. The system is a swept source OCT system with A-line rate of 100,000 Hz. In Fig. 15, a quasi-periodic pattern was caused by phase wrapping, and the phase difference is wrapped between $-\pi$ and π. However, wrapped phase images also give qualitative information regarding acceleration. The absolute value of the velocity can be obtained using the following simple method.

According to Eq. (3), phase difference of $\Delta\theta = 2\pi$ corresponds to a velocity difference of $0.0525m/s$ (here, $\lambda_C = 1.05\mu m$, $\Delta T = 10\mu s$). In Fig. 15, the black striations, as indicated by the white arrows, correspond to a velocity value of $n \times 0.0525m/s$, where n is an integer. The regions with $n = 0$ are decided based upon the peak and valley location of the oscillation. The values for n in the other regions can then be decided by their relative distance to the $n = 0$ region. In Fig. 15, the maximum n is 7, and the maximum velocity is between velocities $0.3675m/s$ and $0.42m/s$, which correspond to n=7 and n=8 respectively. From Fig. 15, we can find that the velocity distribution in the down slope region is different from that in the up slope region. In the down slope, the velocity distribution pattern of the tissue surface is more like a sine function. The velocity changes fast at the peak and valley regions, and it changes slower at the waist region. However, in the up slope, the velocity distribution pattern cannot be seen clearly.

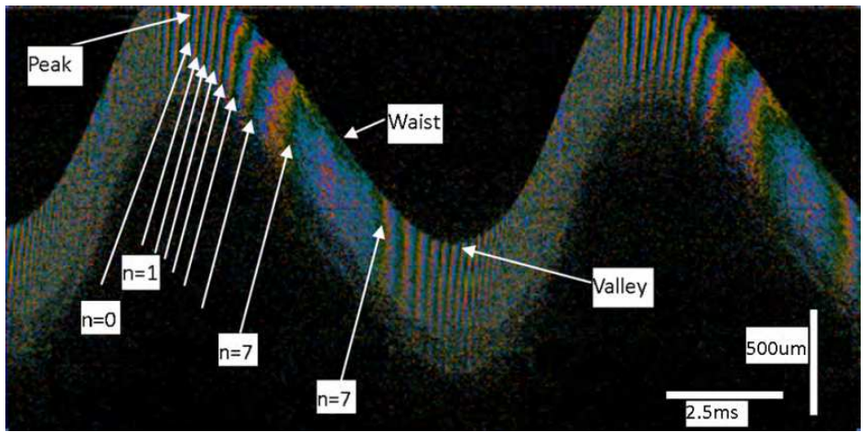

Fig. 15. Color Doppler image of the vibrating vocal fold [19].

7. Summary and conclusions

ODT has seen great improvement since its introduction a decade ago. The development of the phase-resolved method and Fourier domain method has enabled high speed and high sensitivity Doppler imaging in 3D. The sensitivity of PRODT has been improved greatly to provide capillary vascular imaging capability. The application of PRODT has extended to many aspects of biomedical imaging such as ophthalmology, otolaryngology, pulmonology, urology, dermatology and brain imaging. With the advance of OCT technology, the speed and sensitivity of ODT system will improve further, which will enable the applications of ODT technique to more fields. Finally, integration of Doppler OCT with other functional imaging modalities, such as polarization sensitive OCT, spectroscopic OCT, will enhance the potential applications of this technology further.

8. Acknowledgement

The authors thank Elaine Kato for proofreading this manuscript. We thank our former group members, Dr. Yonghua Zhao, Dr. Hongwu Ren, Dr. Lei Wang, Dr. Yimin Wang, Dr. Yi Jiang, Dr. Bin Rao, Dr. Yeh-Chan Ahn, Dr. Woonggyu Jung, Dr. Tuqiang Xie, Dr. Jianping Su, Dr. Lingfeng Yu, our current members, Dr. Jun Zhang, Ms. Wenjuan Qi, Ms. Jiechen Yin,

and all those who have contributed to the Doppler OCT project at the Beckman Laser Institute and Department of Biomedical Engineering at UCI. Dr. Chen also acknowledges grant support from the National Institutes of Health (EB- 00293, NCI-91717, RR-01192, EB-00255 EB-10090, HL-103764 and HL-105215), the National Science Foundation (BES-86924), the Whitaker Foundation (WF-23281), Defense Advanced Research Program Agency (Bioflip program), Air Force Office of Scientific Research (F49620-00-1-0371, FA9550-04-0101), and the Beckman Laser Institute Endowment.

9. References

[1] D. Huang, E. A. Swanson, C. P. Lin, J. S. Schuman, W. G. Stinson, W. Chang, M. R. Hee, T. Flotte, K. Gregory, C. A. Puliafito, and J. G. Fujimoto, "Optical coherence tomography," Science 254, 1178–1181 (1991).

[2] Optical Coherence Tomography: Technology and Applications, Wolfgang Drexler (Editor), James G. Fujimoto (Editor), spinger

[3] V. Gusmeroli and M. Martnelli, "Distributed laser Doppler velocimeter," Opt. Lett. 16, 1358-1360 (1991).

[4] Z. Chen, T. E. Milner, D. Dave, and J. S. Nelson, "Optical Doppler tomographic imaging of fluid flow velocity in highly scattering media," Opt. Lett. 22, 64–66 (1997).

[5] Z. Chen, T. E. Milner, S. Srinivas, X. J. Wang, A. Malekafzali, M. J. C. van Gemert, and J. S. Nelson, "Noninvasive imaging of *in vivo* blood flow velocity using optical Doppler tomography," Opt. Lett. 22, 1119–1121 (1997).

[6] Joseph A. Izatt, Manish D. Kulkarni, Siavash Yazdanfar, Jennifer K. Barton, and Ashley J. Welch, "*In vivo* bidirectional color Doppler flow imaging of picoliter blood volumes using optical coherence tomography," Opt. Lett. 22, 1439-1441 (1997).

[7] Y. Zhao, Z. Chen, C. Saxer, S. Xiang, J. de Boer, and J. Nelson, "Doppler variance imaging for clinical monitoring of *in vivo* human skin blood flow," Opt. Lett. 25, 1358–1360 (2000).

[8] Y. Zhao, Z. Chen, C. Saxer, S. Xiang, J. de Boer, and J. Nelson, "Phase resolved optical coherence tomography and optical Doppler tomography for imaging blood flow in human skin with fast scanning speed and high velocity sensitivity," Opt. Lett. 25, 114–116 (2000).

[9] Y. Zhao, Z. Chen, Z. Ding, H. Ren, and J. S. Nelson, "Three-dimensional reconstruction of in vivo blood vessels in human skin using phase-resolved optical Doppler tomography," IEEE J. of Selected Topics in Quantum Electronics 7, 931-935 (2001).

[10] R. Leitgeb, C. K. Hitzenberger, A. F. Fercher, "Performance of fourier domain vs. Time domain optical coherence tomography," Opt. Express 11, 889-894 (2003), http://www.opticsexpress.org/abstract.cfm?URI=OPEX-11-8-889. [UC-eLinks]

[11] J. F. de Boer, B. Cense, B. H. Park, M. C. Pierce, G. J. Tearney, B. E. Bouma, "Signal to noise gain of spectral domain over time domain optical coherence tomography," Opt. Lett. 28, 2067-2069 (2003). [UC-eLinks]

[12] M. A. Choma, M. V. Sarunic, C. Yang,J. A. Izatt, "Sensitivity advantage of swept source and fourier domain optical coherence tomography," Opt. Express 11, 2183-2189 (2003),

[13] R.A. Leitgeb, L. Schmetterer, W. Drexler, A.F. Fercher, R.J. Zawadzki, T. Bajraszewski, Opt. Exp. 11, 3116 (2003)
[14] B.R. White, M.C. Pierce, N. Nassif, B. Cense, B.H. Park, G.J. Tearney, B.E. Bouma, T.C. Chen, J.F. de Boer, Opt. Exp. 25, 3490 (2003)
[15] L. Wang, Y. Wang, M. Bachaman, G.P. Li, Z. Chen, Opt. Commun. 242, 345 (2004)
[16] Jun Zhang and Zhongping Chen, "In vivo blood flow imaging by a swept laser source based Fourier domain optical Doppler tomography," Opt. Express 13, 7449-7457 (2005) http://www.opticsinfobase.org/abstract.cfm?URI=oe-13-19-7449
[17] B. Vakoc, S. Yun, J. de Boer, G. Tearney, and B. Bouma, "Phase-resolved optical frequency domain imaging," Opt. Express 13, 5483-5493 (2005) http://www.opticsinfobase.org/abstract.cfm?URI=oe-13-14-5483
[18] Desmond C. Adler, Robert Huber, and James G. Fujimoto, "Phase-sensitive optical coherence tomography at up to 370,000 lines per second using buffered Fourier domain mode-locked lasers," Opt. Lett. 32, 626-628 (2007) http://www.opticsinfobase.org/abstract.cfm?URI=ol-32-6-626
[19] Gangjun Liu, Marc Rubinstein, Arya Saidi, Wenjuan Qi, Allen Foulad, Brian Wong and Zhongping Chen, "Imaging vocal fold vibration with a high speed 1um swept source OCT and ODT system," *Optics Express*, 19, 11880–11889 (2011).
[20] Gangjun Liu, Lidek Chou, Wangcun Jia, Wenjuan Qi, Bernard Choi, and Zhongping Chen, "Intensity-based modified Doppler variance algorithm: application to phase instable and phase stable optical coherence tomography systems," *Optics Express*, 19, 11429–11440 (2011).
[21] Ruikang K. Wang and Zhenhe Ma, "Real-time flow imaging by removing texture pattern artifacts in spectral-domain optical Doppler tomography," Opt. Lett. 31, 3001-3003 (2006) http://www.opticsinfobase.org/abstract.cfm?URI=ol-31-20-3001
[22] Hongwu Ren, Tao Sun, Daniel J. MacDonald, Michael J. Cobb, and Xingde Li, "Real-time in vivo blood-flow imaging by moving-scatterer-sensitive spectral-domain optical Doppler tomography," Opt. Lett. 31, 927-929 (2006) http://www.opticsinfobase.org/abstract.cfm?URI=ol-31-7-927
[23] J. Fingler, R. J. Zawadzki, J. S. Werner, D.Schwartz, and S. E. Fraser, "Volumetric microvascular imaging of human retina using optical coherence tomography with a novel motion contrast technique," Opt. Express 17, 22190-22200 (2009). http://www.opticsinfobase.org/abstract.cfm?URI=oe-17-24-22190
[24] L. An, J. Qin, and R. K. Wang, "Ultrahigh sensitive optical microangiography for in vivo imaging of microcirculations within human skin tissue beds," Optics Express 18, 8220-8228 (2010).
[25] Yeongri Jung, Zhongwei Zhi and Ruikang K. Wang, "Three-dimensional optical imaging of microvascular networks within intact lymph node *in vivo*", J. Biomed. Opt. 15, 050501
[26] S. Zotter, M. Pircher, T. Torzicky, M. Bonesi, E. Götzinger, R. A. Leitgeb, and C. K. Hitzenberger, "Visualization of microvasculature by dual-beam phase-resolved Doppler optical coherence tomography," Opt. Express 19, 1217-1227 (2011). http://www.opticsinfobase.org/abstract.cfm?URI=oe-19-2-1217

[27] S. Makita, F. Jaillon, M. Yamanari, M. Miura, and Y. Yasuno, "Comprehensive in vivo micro-vascular imaging of the human eye by dual-beam-scan Doppler optical coherence angiography," Opt. Express 19, 1271-1283 (2011). http://www.opticsinfobase.org/abstract.cfm?URI=oe-19-2-1271

[28] David H. Evans, W. Norman McDicken, Doppler Ultrasound: Physics, Instrumental, and Clinical Applications, 2nd Edition (John Wiley Sons, 2000)

[29] H. Ren, K. M. Brecke, Z. Ding, Y. Zhao, J. S. Nelson, and Z. Chen, "Imaging and quantifying transverse flow velocity with the Doppler bandwidth in a phase-resolved functional optical coherence tomography," Opt. Lett. 27, 409-411 (2002). http://www.opticsinfobase.org/abstract.cfm?URI=ol-27-6-409

[30] H. Ren, Y. Wang, J. S. Nelson, and Z. Chen, "Power optical Doppler tomography imaging of blood vessel in human skin and M-mode Doppler imaging of blood flow in chick chrioallantoic membrane," in Coherence Domain Optical Methods and Optical Coherence Tomography in Biomedicine VII, V. V. Tuchin, J. A. Izatt, and J. G. Fujimoto, eds., Proc. SPIE 4956, 225-231 (2003).

[31] R. K.Wang, S. L. Jacques, Z. Ma, S. Hurst, S. R. Hanson, and A. Gruber, "Three dimensional optical angiography," Optics Express, vol. 15, no. 7, pp. 4083–4097, 2007.

[32] R. K. Wang and S. Hurst, "Mapping of cerebro-vascularblood perfusion in mice with skin and skull intact by Optical Micro-AngioGraphy at 1.3 μm wavelength," Optics Express, vol. 15, no. 18, pp. 11402–11412, 2007.

[33] L. An and R. K. Wang, "In vivo volumetric imaging of vascular perfusion within human retina and choroids with optical micro-angiography," Optics Express, vol. 16, no. 15, pp. 11438–11452, 2008.

[34] R. K. Wang and L. An, "Doppler optical micro-angiography for volumetric imaging of vascular perfusion in vivo," Optics Express, vol. 17, no. 11, pp. 8926–8940, 2009.

[35] L. An, H. M. Subhash, D. J. Wilson, and R. K. Wang, "High resolution wide-field imaging of retinal and choroidal blood perfusion with optical micro-angiography," Journal of Biomedical Optics, vol. 15, no. 2, 2010.

[36] Z. Yuan, Z. C. Luo,H. G. Ren, C.W. Du, and Y. Pan, "A digital frequency ramping method for enhancing Doppler flow imaging in Fourier-domain optical coherence tomography," *Optics Express*, vol. 17, no. 5, pp. 3951–3963, 2009.

[37] Yuankai K. Tao, Anjul M. Davis, and Joseph A. Izatt, "Single-pass volumetric bidirectional blood flow imaging spectral domain optical coherence tomography using a modified Hilbert transform," Opt. Express 16, 12350-12361 (2008) http://www.opticsinfobase.org/abstract.cfm?URI=oe-16-16-12350

[38] Yuankai K. Tao, Kristen M. Kennedy, and Joseph A. Izatt, " Velocity-resolved 3D retinal microvessel imaging using single-pass flow imaging spectral domain optical coherence tomography," Opt. Express 17, 4177-4188 (2009) . http://www.opticsinfobase.org/abstract.cfm?uri=oe-17-5-4177

[39] C. Kasai, K. Namekawa, A. Koyano, R. Omoto, "Real-Time Two-Dimensional Blood Flow Imaging Using an Autocorrelation Technique," IEEE Trans. Sonics Ultrason, SU-32(3), 458-464(1985).

[40] V. X. Yang, M. L. Gordon, A. Mok, Y. Zhao, Z. Chen, R. S. Cobbold, B. C. Wilson, and I. A. Vitkin, "Improved phase-resolved optical Doppler tomography using Kasai velocity estimator and histogram segmentation," Opt. Commun. 208, 209-214 (2002)

[41] Lingfeng Yu and Zhongping Chen, “Doppler variance imaging for three-dimensional retina and choroid angiography,” J. Biomed. Opt. 15, 016029 (2010)

[42] Gangjun Liu, Wenjuan Qi, Lingfeng Yu, and Zhongping Chen, "Real-time bulk-motion-correction free Doppler variance optical coherence tomography for choroidal capillary vasculature imaging," Opt. Express 19, 3657-3666 (2011) http://www.opticsinfobase.org/abstract.cfm?URI=oe-19-4-3657

[43] Z. Chen, Y. Zhao, S. M. Srivivas, J. S. Nelson, N. Prakash, and R. D. Frostig, “Optical Doppler Tomography,” IEEE J. Select. Topics Quantum Electro. 5, 1134 (1999).

[44] Z. Chen, T. E. Milner, S. Srinivas, A. Malekafzali, X. Wang, M. J. C. Van Gemert, J. S. Nelson, “Characterization of Blood Flow Dynamics and Tissue Structure Using Optical Doppler Tomography,” Photochemistry and Photobiology 67, 56-60 (1998).

[45] Bin Rao, Lingfeng Yu, Huihua Kenny Chiang, Leandro C. Zacharias, Ronald M. Kurtz, Baruch D. Kuppermann and Zhongping Chen,"Imaging pulsatile retinal blood flow in human eye", JBO Letters, 040505(2008).

[46] J. Nelson, K. Kelly, Y. Zhao, and Z. Chen, “Imaging blood flow in human port wine stain in situ and in real time using optical Doppler tomography”, Archives of Dermatology, 137, 741-4 (2001).

[47] Vakoc BJ, Lanning RM, Tyrrell JA, Padera TP, Bartlett LA, Stylianopoulos T, Munn LL, Tearney GJ, Fukumura D, Jain RK, Bouma BE. Three-dimensional microscopy of the tumor microenvironment in vivo using optical frequency domain imaging. Nat Med. 2009 Oct;15(10):1219-23.

[48] Vivek J. Srinivasan, Sava Sakadžić, Iwona Gorczynska, Svetlana Ruvinskaya, Weicheng Wu, James G. Fujimoto, and David A. Boas, "Quantitative cerebral blood flow with Optical Coherence Tomography," Opt. Express 18, 2477-2494 (2010) http://www.opticsinfobase.org/abstract.cfm?URI=oe-18-3-2477

[49] Shuichi Makita, Youngjoo Hong, Masahiro Yamanari, Toyohiko Yatagai, and Yoshiaki Yasuno, “Optical coherence angiography,” Opt. Express 14, 7821(2006). http://www.opticsinfobase.org/abstract.cfm?URI=oe-14-17-7821

[50] HrebeshM. Subhash, “Biophotonics Modalities for High-Resolution Imaging of Microcirculatory Tissue Beds Using Endogenous Contrast: A Review on Present Scenario and Prospects”, International Journal of Optics, Article ID 293684 (2011).

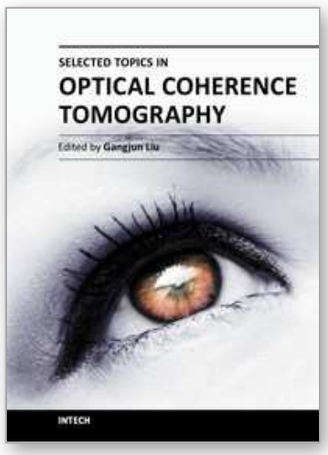

Selected Topics in Optical Coherence Tomography

Edited by Dr. Gangjun Liu

ISBN 978-953-51-0034-8
Hard cover, 280 pages
Publisher InTech
Published online 08, February, 2012
Published in print edition February, 2012

This book includes different exciting topics in the OCT fields, written by experts from all over the world. Technological developments, as well as clinical and industrial applications are covered. Some interesting topics like the ultrahigh resolution OCT, the functional extension of OCT and the full field OCT are reviewed, and the applications of OCT in ophthalmology, cardiology and dentistry are also addressed. I believe that a broad range of readers, such as students, researchers and physicians will benefit from this book.

How to reference

In order to correctly reference this scholarly work, feel free to copy and paste the following:

Gangjun Liu and Zhongping Chen (2012). Phase-Resolved Doppler Optical Coherence Tomography, Selected Topics in Optical Coherence Tomography, Dr. Gangjun Liu (Ed.), ISBN: 978-953-51-0034-8, InTech, Available from: http://www.intechopen.com/books/selected-topics-in-optical-coherence-tomography/phase-resolved-doppler-optical-coherence-tomography

INTECH
open science | open minds

InTech Europe
University Campus STeP Ri
Slavka Krautzeka 83/A
51000 Rijeka, Croatia
Phone: +385 (51) 770 447
Fax: +385 (51) 686 166
www.intechopen.com

InTech China
Unit 405, Office Block, Hotel Equatorial Shanghai
No.65, Yan An Road (West), Shanghai, 200040, China
中国上海市延安西路65号上海国际贵都大饭店办公楼405单元
Phone: +86-21-62489820
Fax: +86-21-62489821

IntechOpen